Wave Normal Shock," *AIAA Journal*, Vol. 7, No. 7, July 1969, pp. 1335–1344.

[12] Busch, C. W., Laderman, A. J., and Oppenheim, A. K., "Pressure Wave Generation in Particle-Fueled Combustion Systems: I. Parametric Study," *AIAA Journal*, Vol. 4, No. 9, Sept. 1966, pp. 1638–1644.

[13] Busch, C. W. et al., "Pressure Wave Generation in Particle Fueled Combustion Systems: II. Influence of Particle Motion," *AIAA Journal*, Vol. 6, No. 2, Feb. 1968, pp. 286–291.

[14] Smith, H. P., Jr., Busch, C. W., and Oppenheim, A. K., "Pressure Wave Generated in a Fissionable Gas by Neutron Irradiation," *The Physics of Fluids*, Vol. 7, No. 5, May 1964, pp. 676–682.

[15] Smith, Jr., H. P., Evans, R. D., Busch, C. W. and Oppenheim, A. K., "Pressure Wave Generation in a Fissioning Gas: II. Effects of Dissociation and Multiphase Composition," *The Physics of Fluids*, Vol. 8, No. 8, Aug. 1965, pp. 1421–1423.

[16] Busch, C. W., Oppenheim, A. K., and Smith, H. P., Jr., "Pressure Wave Generation in a Fissioning Gas: III. Amplification of the Pressure Pulse with Helium 3 as Driver," *The Physics of Fluids*, Vol. 9, No. 4, April 1966, pp. 813–814.

[17] Podney, W. N., Smith, Jr., H. P., and Oppenheim, A. K., "On the Generation of a Fissioning Plasma in a Shock Tube," *Proceedings of the Sixth International Shock Tube Symposium*, Freiburg, April 1967; also *The Physics of Fluids*, Vol. 12, No. 15, May 1969, pp. I 68–I 72.

[18] Stull, D. R., "JANAF Thermochemical Tables," The Thermal Research Lab., Aug. 1965, Dow Chemical Co., Midland, Mich.

[19] Rudinger, G., *Wave Diagrams for Nonsteady Flow in Ducts*, D. Van Nostrand, New York, 1955.

[20] Skinner, G. B. and Ringrose, G. H., "Ignition Delays of a Hydrogen-Oxygen-Argon Mixture at Relatively Low Temperatures," *Journal of the Chemical Society (London)*, Vol. 42, No. 6, June 1965, pp. 2190–2192.

[21] Hirsch, E. and Ryason, P. R., "A Study of the Hydrogen-Oxygen Reaction," *The Journal of Chemical Physics*, Vol. 40, No. 7, April 1964, pp. 2050–2051.

[22] Shapiro, A. H., *The Dynamics and Thermodynamics of Compressible Fluid Flow*, Vol. II, Chaps. 24 and 25, Ronald Press, New York, 1953.

[23] Korn, G. A. and Korn, T. M., *Mathematical Handbook for Scientists and Engineers*, McGraw-Hill, New York, 1961.

[24] Zajac, L. J. and Oppenheim, A. K., "Thermodynamic Computations for the Gasdynamic Analysis of Explosion Phenomena," *Combustion and Flame*, Vol. 13, No. 5, Oct. 1969, pp. 537–550.

[25] Fristrom, R. M. and Westenberg, A. A., *Flame Structure*, McGraw-Hill, New York, 1965, p. 281.

APRIL 1971 AIAA JOURNAL VOL. 9, NO. 4

Coupled Nongray Radiating Flows about Long Blunt Bodies

LINWOOD B. CALLIS*
NASA Langley Research Center, Hampton, Va.

Second-order time asymptotic solutions extending far downstream are presented for hypervelocity blunt-body flowfields including coupled nongray radiation. Shapes considered are sphere-cones and blunted conical shapes with continuous curvature. Numerical calculations treat the shock as a discrete surface, and it is assumed that the flow is inviscid, nonconducting, and axisymmetric. Thermochemical equilibrium is assumed. Radiation is accounted for with an eight-step model absorption coefficient including line, band, and continuum radiation. Results include shock shapes, radiative heating distributions, and profiles through the shock layer of pertinent thermodynamic and flow quantities. A parametric analysis is made of radiating flows over sphere-cones. Comparisons with other investigators are made, where possible.

Nomenclature

A,B,C,D,E = defined by Eq. (5)
B_ν = nondimensional blackbody function
$\bar{c}$ = speed of light, m/sec
E_n = exponential integral function of order n, $E_n(y) = \int_1^\infty e^{-yt}\, t^{-n}\, dt$
F^R = nondimensional divergence of the radiation flux vector
g = general parameter representing ρ,u,v, or p
h = nondimensional enthalpy
$\bar{h}_P$ = Planck's constant, joule-sec
I_ν = nondimensional specific radiation intensity
K = defined by Eqs. (5)
$\bar{k}$ = Boltzmann constant, joules/°K
P_1,P_3 = defined by Eqs. (5)
p = nondimensional pressure
q^R = nondimensional radiative heat flux to body
$\bar{R}_N$ = nose radius, m
r = nondimensional radial coordinate
s = nondimensional radiation path length
T = nondimensional temperature where indicated
T,t',t = nondimensional time
u,v = nondimensional velocity components, body-oriented system
$\bar{V}_\infty$ = freestream velocity, m/sec
x,y = nondimensional body-oriented coordinates
x',y' = nondimensional Cartesian coordinates
X,Y = nondimensional floating coordinates
$\bar{Z}$ = altitude, km
β = local shock angle relative to body, radians
δ = nondimensional standoff distance
ϵ = defined by Eqs. (5)
θ = body surface inclination, rad
λ = defined by Eqs. (5)
ν = nondimensional radiation frequency
ρ = nondimensional density
ρk = nondimensional absorption coefficient
ρk_P = nondimensional Planck mean absorption coefficient
$\bar{\sigma}$ = Stefan-Boltzmann constant, $w/(m^2 - °K^4)$
τ = optical thickness
ω = solid angle

Subscripts

c = asymptotic or conical angle
o = standard conditions
st = stagnation conditions

Presented as Paper 70-865 at the AIAA 5th Thermophysics Conference, Los Angeles, Calif., June 29–July 1, 1970; submitted July 31, 1970; revision received October 22, 1970.

* Aero-Space Technologist, Gas Radiation Section, Hypersonic Vehicles Division.

Δ = stationary normal shock conditions
δ = local shock conditions
∞ = freestream conditions

Introduction

THERE are currently available a number of reliable numerical solutions[1-5] for predicting radiative heating rates at blunt-body stagnation points. These solutions are fully coupled and, with varying degrees of approximation, include the effect of nongray emission and absorption of radiation. Viscous effects are included by Wilson and Hoshizaki[5] and the effects of ablation are treated by Chin[3] and Wilson and Hoshizaki.[5] Indeed, techniques have so advanced that, aside from refinements in the absorption coefficients used, the prediction of equilibrium stagnation-point radiative heating rates with no ablation no longer poses a major problem. For an analysis with ablation, however, work needs to be done to determine more precisely what ablated vapor species are present and what the absorption coefficients of such species are.

The case for the downstream regions of the flowfield, with or without ablation, is not so well advanced. To date, work dealing with nonadiabatic effects due to radiation downstream of the stagnation point has either been concerned with or restricted to inverse problems, integral techniques, decoupled flows, gray or transparent gases, the subsonic portion of the flow field, or sharp cones and wedges.[6-11] One of the most fruitful efforts to determine the downstream effect of coupled radiation was the work of Olstad.[7] With a flowfield technique devised by Maslen[12] and modified to account for nongray radiation, Olstad studied nonadiabatic flows with and without large blowing, past a family of blunted cones with continuous curvature. The solutions extend well into the supersonic flow region and provide valuable insight concerning the downstream effects of radiation. It should be noted, however, that the Maslen technique is an inverse solution, proceeding from a specified shock, and that the assumptions which give the technique its utility are not strictly valid near the stagnation line. As a result, errors in that region may be significant.

The present paper has two purposes. The first is to present a solution for radiating flow fields *embodying none of the limitations mentioned in the preceding paragraph.* The solution is essentially the second-order time asymptotic technique reported by the author[1] applied downstream of the stagnation point. Simply expressed, the technique advances an assumed solution through successive time increments according to a second-order Taylor series expansion in time. The process is continued until a situation is reached invariant with time which represents the steady-state result. Shock waves, with the aid of unsteady characteristics, are treated as discontinuities.

There are compelling reasons for choosing such a technique to achieve a solution. First, since the set of unsteady governing equations is hyperbolic, the same computational methods may be used in both the subsonic and supersonic flow regions. This permits a single, direct solution to extend from the stagnation line, far downstream of the sonic line. Second, the stability criterion for the numerical solution of hyperbolic equations is well known and instabilities present no problem. Finally, the completed solution is achieved with a moderate amount of computer time ($\sim$5 min, CDC 6600) and core storage (100,000 words) and is, within reason, insensitive to the flowfield assumed to initiate the solution. These factors, coupled with the accuracy of the solution, form a persuasive argument for the use of such techniques for flowfield analysis.

The second purpose of this paper is to present and discuss the solutions to radiating flowfields over blunt bodies. These solutions include the effect of the emission and absorption of coupled nongray radiation throughout the entire flowfield. Calculation of radiative effects are facilitated with the use of an eight-step model absorption coefficient formulated by Olstad.[7] In this model, line, band, and continuum radiation are taken into account. Results discussed consist of distributions around the body and profiles through the shock layer of the radiative heat transfer and pertinent flow and thermodynamic properties.

Analysis

In order to avoid repetition, the following section of this paper will present brief, descriptive but not detailed, comments regarding the various facets of the governing equations and their general application. A more complete development and discussion is given by the author in Ref. 1.

Nondimensionalization

The equations appearing in this paper have been nondimensionalized as follows: distances by $\bar{R}_N$, time quantities by the ratio $\bar{R}_N/\bar{V}_\infty$, densities by $\bar{\rho}_\infty$, pressures by $\bar{\rho}_\infty \bar{V}_\infty{}^2$, energy fluxes by $\frac{1}{2}\bar{\rho}_\infty \bar{V}_\infty{}^3$, enthalpies by $\bar{V}_\infty{}^2$, the divergence of the radiation flux vector by $\bar{\sigma}(\bar{\rho}\bar{k}_P)_\Delta \bar{T}_\Delta{}^4$ where $\bar{T}_\Delta$ is a temperature, velocities by V_∞, and absorption coefficients by $(\bar{\rho}\bar{k}_P)_\Delta$. Barred quantities, where present, are dimensional.

Basic Assumptions and Flow Model

The assumptions upon which this analysis rests are that 1) the flow is axisymmetric, inviscid, and nonconducting; 2) the flow is in thermochemical equilibrium; 3) the shock wave and freestream are transparent to shock-layer radiation; 4) the body surface, with regard to radiation, is cold, black, and nonreflecting; and 5) for radiation effects, the tangent slab approximation is applicable. These assumptions simplify the problem and permit radiation effects on the downstream flowfield to be depicted clearly. Figure 1 presents a schematic illustration of the flow geometry about a blunted conical vehicle.

Governing Equations

The unsteady, inviscid, nonconducting equations governing the present analysis are given in nondimensional form as: Continuity

$$\rho_T = -[A\rho_Y + (u/\lambda)\rho_X - Bu_Y + \rho u_X/\lambda + \rho v_Y/\delta + C] \tag{1}$$

X momentum

$$u_T = -[Au_Y + uu_X/\lambda - (B/\rho^2)p_Y + p_X/\rho\lambda + D] \tag{2}$$

Y momentum

$$v_T = -[Av_Y + (u/\lambda)v_X + p_Y/\rho\delta - E] \tag{3}$$

Energy

$$p_T = -\left(Ap_Y + \frac{u}{\lambda}p_X + P_3\left[\frac{\rho}{\lambda}u_X - Bu_Y + \frac{\rho}{\delta}v_Y + C\right] - \frac{\epsilon F^R}{P_1\rho}\right) \tag{4}$$

where, with the aid of the state equation, the energy equation has been written in terms of pressure rather than enthalpy. Subscript notation has been used to denote partial differentiation. The parameters in Eqs. (1-4) are defined by the following relations

$$A = v/\delta - Y\delta_T/\delta - (uY/\delta)\tan\beta\,\lambda_\delta/\lambda \tag{5a}$$

$$B = (\lambda_\delta/\lambda)(\rho Y/\delta)\tan\beta \tag{5b}$$

$$C = (\rho u/r)\sin\theta + \rho v[K/\lambda + (\cos\theta)/r] \tag{5c}$$

$$D = Kuv/\lambda \tag{5d}$$

$$E = Ku^2/\lambda \tag{5e}$$

$$P_3 = (\partial h/\partial\rho)_p/[1/\rho - (\partial h/\partial p)_\rho] \tag{5f}$$

$$P_1 = 1/\rho - (\partial h/\partial p)_\rho \tag{5g}$$

$$\lambda = 1 + Ky \tag{5h}$$

$$K = -d\theta/dx \tag{5j}$$

$$\epsilon = \bar{\sigma}\bar{R}_N(\bar{\rho}\bar{k}_P)_\Delta\bar{T}_\Delta{}^4/\bar{p}_\infty\bar{V}_\infty{}^3 \tag{5k}$$

In the application of Eqs. (1–5) to center-line flow ($r = 0$), indeterminate expressions such as $\rho u \sin\theta/r$ have been evaluated with the aid of L'Hospital's rule.

Equations (1–4) are the familiar body-oriented equations of motion transformed according to

$$T = t, \quad X = x, \quad Y = y/\delta \tag{6}$$

Body-oriented coordinates are not convenient for unsteady analysis. This is due to the moving shock wave passing through the fixed mesh points causing differencing difficulties in the vicinity of the shock, and changing the number of mesh points used to describe the shock layer. The transformation to the "floating" coordinate system by Eqs. (6) eliminates these problems since both the shock and the body become coordinate lines. In addition, the transformation is such that the relative distribution of mesh points in the shock layer is constant regardless of the motion of the shock. A schematic of the floating coordinate system is shown on Fig. 1.

The present time asymptotic approach uses a Taylor series expansion in time,

$$g(X,Y,T + \Delta T) = g(X,Y,T) + g_T(X,Y,T)\Delta T + \tfrac{1}{2}g_{TT}(X,Y,T)\Delta T^2 + 0(\Delta T^3) \tag{7}$$

The expansion furnishes a new value of the parameter g, which may represent p,ρ,u, or v at X,Y, and $T + \Delta T$. This procedure is carried out at each mesh point until the information necessary for the continuation of the solution in time is available at $T + \Delta T$. Information on the shock wave and body at $T + \Delta T$ is generated with the aid of unsteady characteristics, discussed in a later section. Once a new time plane is completely determined, the process is repeated until a converged, or steady-state, solution is reached.

The first-order time derivatives required in Eq. (7) are determined from Eqs. (1–4). Second-order time derivatives are evaluated using these same equations in conjunction with the identities

$$g_{TT}(X,Y,T) = (\partial/\partial T)[g_T(X,Y,T)] \tag{8}$$

$$(\partial/\partial T)[g_X(X,Y,T)] = (\partial/\partial X)[g_T(X,Y,T)] \tag{9}$$

and

$$(\partial/\partial T)[g_Y(X,Y,T)] = (\partial/\partial Y)[g_T(X,Y,T)] \tag{10}$$

All space derivatives appearing in Eqs. (1–4) and (8–10) are determined by a "centered type" of finite difference representation with the exception of points on boundaries. At these points, forward or backward difference representations were used. The time derivatives of the parameters defined by Eqs. (5) are represented by backward differences in time. This use of backward time differencing is consistent with the maintenance of second-order accuracy since these derivatives appear only in the second-order terms of Eq. (7). Hence, neglected terms are of third order.

Equations (1–5, 7–10), and the system of unsteady characteristic relations form a determinant set from which, barring numerical instabilities, a converged solution may be obtained.

The stability requirement applied to the present analysis is the Courant-Friedricks-Lewy (CFL) criterion used by Moretti,[13]

$$\Delta T \leq \{(\Delta X,\Delta Y)/[(u,v) + P_3{}^{1/2}]\}_{\min} \tag{11}$$

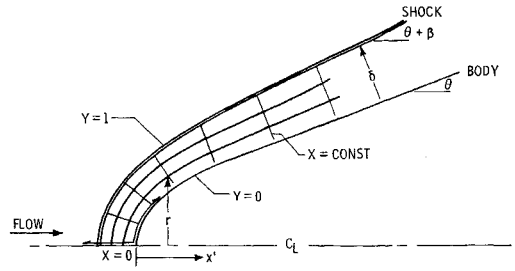

Fig. 1 Schematic of flowfield and coordinate system.

Clearly, the allowable time increment is directly coupled to the size of the solution mesh, as is the execution time of the numerical program. In an effort to extend the solutions far downstream and reduce the time and storage requirements, a mesh stretched in the body tangent direction has been employed. The degree of stretching is related to the longitudinal radius of curvature of the body so that in regions of high body curvature, where flow properties can be expected to vary more rapidly, the mesh points are relatively closely spaced, furnishing the information and accuracy needed in this flow region. As the curvature decreases the grid spacing increases, resulting in large savings of both computer time and storage. The centered finite difference representation of the spatial derivatives has been modified to account for nonuniformities in mesh spacing.

For maximum accuracy with such a mesh, the CFL criterion, due to its large variation over a long body, must be applied locally with the solution at each mesh point advancing in time as far as permitted. The data must subsequently be "leveled" after each time step to a common time plane defined by the smallest time increment. This is done with a linear interpolation in time. Such a procedure was necessary to avoid errors resulting from the imposition of the most stringent time step in the flowfield at a point where a significantly larger time step is permissible (see Ames,[14] Chap. 7). Such errors, if permitted, would not result in instabilities but would render the solution nonconvergent. Local application of the stability criterion is effective in eliminating this source of error.

The divergence of the radiative flux vector F^R which appears in the energy equation is given by

$$F^R = \int_0^\infty \int_0^{4\pi} \frac{\partial I_\nu}{\partial s}\, d\omega d\nu \tag{12}$$

where I_ν is the specific intensity of the radiation and ds an incremental length along the path the radiation travels. With the aid of the radiative transfer equation and the adopted step model absorption coefficient, and assuming that the tangent slab approximation is applicable and that $dT^4/d\tau$ is constant between mesh points, Eq. (12) may be integrated to give

$$F_{k,L}{}^R = \Big\{4\,(\rho k_p)_k T_k{}^4 - 2\sum_{i=1}^{N}(\rho k_i)_k \times \Big(2(T_{i,k}{}^*)^4 - (T_{i,1}{}^*)^4 E_2(\tau_{i,k}) - (T_{i,M+1}{}^*)^4 E_2(|\tau_{i,M+1} - \tau_{i,k}|) - \sum_{j=1}^{M}\Big[\Big\{\frac{(T_{i,j+1}{}^*)^4 - (T_{i,j}{}^*)^4}{\Delta t_{i,j}}\Big\}[E_3(|\tau_{i,j+1} - \tau_{i,k}|) - E_3(|\tau_{i,j} - \tau_{i,k}|)]\Big]\Big)\Big\}_L \tag{13a}$$

$$L = 1 \ldots L_T \tag{13b}$$

$$k = 1 \ldots M + 1 \tag{13c}$$

where there are N steps in the absorption coefficient, $M + 1$ mesh points across the shock layer, L_T mesh points around

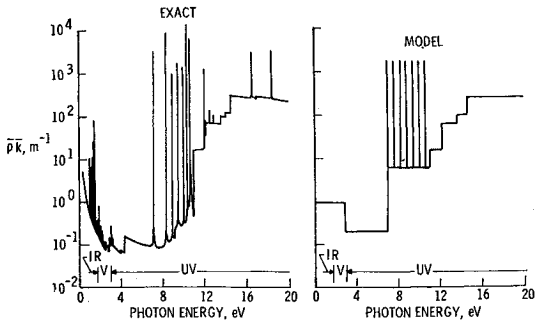

Fig. 2 Schematic of exact and model absorption coefficient.

the body and where

$$\Delta t_{i,j} = \tau_{i,j+1} - \tau_{i,j} \tag{14}$$

$$T_{i,j}{}^{*} = \eta_{i,j}{}^{0.25} T_j \tag{15}$$

$$\eta_{i,j} = \int_{\Delta\nu i} (B_{\nu,j}\, d\nu)/(T^4/\pi)_j \tag{16a}$$

$$B\nu\, d\nu = \left\{ \frac{2\bar{h}_P \bar{\nu}^3}{\bar{c}^2} \frac{d\bar{\nu}}{(e^{\bar{h}_P \bar{\nu}/\bar{k}\bar{T}} - 1)} \right\} \Big/ \bar{\sigma} \bar{T}_\Delta{}^4 \tag{16b}$$

T being a temperature. The subscript k refers to the kth mesh point across the shock layer and i to the ith step in the model absorption coefficient. In a similar manner, the radiative heat transfer to the body is shown to be

$$q_L{}^R = \frac{4\bar{\sigma}\bar{T}_\Delta{}^4}{\bar{\rho}_\infty \bar{V}_\infty{}^3} \left(\sum_{i=1}^{N} \left\{ \frac{(T_{i,1}{}^{*})^4}{2} - (T_{i,M+1}{}^{*})^4 E_3(\tau_{i,M+1}) - \sum_{j=1}^{M} \frac{(T_{i,j+1}{}^{*})^4 - (T_{i,j}{}^{*})^4}{\Delta t_{i,j}} [E_4(\tau_{i,j+1}) - E_4(\tau_{i,j})] \right\} \right)_L \tag{17a}$$

$$L = 1 \ldots L_T \tag{17b}$$

Solution for Shock and Body Points

Shock points and body points, in this solution, are determined by the quasi-one-dimensional method of unsteady characteristics. This technique, discussed fully by the present author in Ref. 1, will not be detailed in this paper. The method is used, however, because it retains the discontinuous nature of the shock wave providing more accurate solution profiles in the vicinity of the shock front. Methods employing artificial viscosity (Lax,[15] and Lax and Wendroff[16]) calculate shock waves as an inherent part of the flow-field smearing the shock profile over several mesh points. To retain definition in such calculations, a small mesh is required necessitating proportionately smaller time steps and increasing both the execution time and core storage required. Use of the method-of-characteristics permits larger mesh spacing avoiding both these problems.

Absorption Coefficient Model and Gas Properties

With the inclusion of coupled radiation in the flowfield calculations, the additional complexity and time consumed is directly proportional to the complexity of the absorption coefficient used. If a true replica (including line, band, and continuum contributions) of the absorption coefficient is employed in the calculation of F^R, practical flowfield calculations become prohibitive. The approach adopted in this analysis is to use a step model absorption coefficient, the steps of which are functions of temperature and density. References 1 and 17 show that a carefully chosen model of this type can be used with the retention of good accuracy and all significant trends.

The particular model used is an eight-step model, developed by Olstad,[7] including line, band, and continuum radiation. In the vacuum ultraviolet, contributions to the absorption of radiation due to electron recombination were obtained from Hahne.[18] Relations describing the ultraviolet line contributions to the absorption coefficient were obtained by curve fitting the tabulated values of Ref. 2 and multiplying by a factor of 20. This correction was applied because the f numbers on which the values in Ref. 2 were based were shown by Wilson and Nicolet[19] to be too small on the average by a factor of about 20. Data tabulated by Page[4] et al. were used for the continuum in the visible portion of the spectrum, and for lines in the infrared.† The absorption due to line radiation was incorporated in the step model with the aid of a "picket fence" representation consisting of two steps. The first step, really an effective step, is composed of a large number of tall thin steps of equal height, width, and spacing. This "group of steps" is considered collectively and is superposed on a uniform gray background between 911 Å and 1800 Å. The two steps together describe the line radiation in the vacuum ultraviolet. Figure 2 is a schematic of the "exact" and modeled absorption coefficients.

Equilibrium air correlations used in this paper are presented by Cohen[20,21] or have been derived from data presented therein. More exact data, either tabulated or calculated, were not used in an effort to save computational time and in the interest of program simplicity. With regard to the general accuracy of the over-all solution, it is felt that uncertainties in the absorption coefficient information generally available outweigh errors due to the use of thermodynamic correlations.

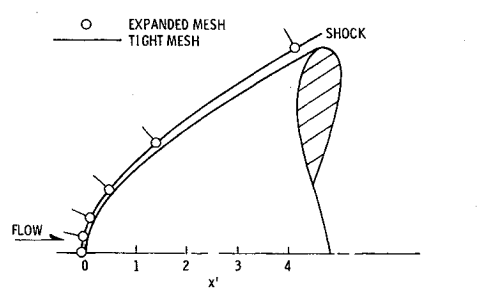

Fig. 3 Comparison of shock shapes for expanded and tight mesh; $\bar{V}_\infty$ = 14 km/sec, $\bar{\rho}_\infty/\bar{\rho}_0 = 10^{-3}$, $\bar{R}_N$ = 2 m, and ϵ = 0.

Results and Discussion

This section will discuss the suitability of the present technique for full flowfield calculations and will present results of long blunt-body flowfield analyses including the effects of downstream radiation.

In the analysis section, it was pointed out that a stretched mesh was introduced permitting calculations to extend far downstream of the sonic line. Figure 3 presents a comparison of solutions, with $\epsilon = 0$ (i.e., for no radiation), achieved

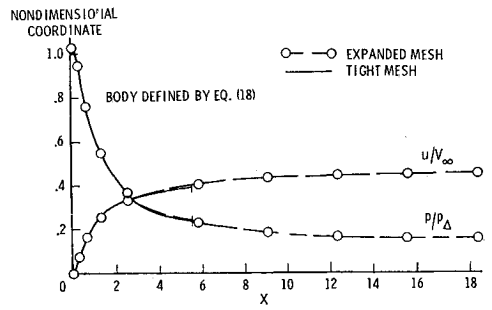

Fig. 4 Comparison of pressure and tangential velocity distribution for expanded and tight mesh; $\bar{V}^\infty$ = 14 km/sec, $\bar{\rho}_\infty/\bar{\rho}_0 = 10^{-3}$, $\bar{R}_N$ = 2 m, and ϵ = 0.

† D. L. Compton of NASA Ames Research Center pointed out an error in the use of a portion of this data. The effect of this error in the present analysis, however, is insignificant.

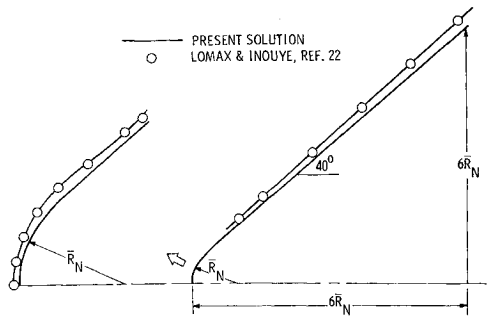

Fig. 5 Comparison of shock shapes for 40° sphere-cone; $\bar{V}_\infty$ = 12.2 km/sec, $\bar{\rho}_\infty/\bar{\rho}_0 = 2.24 \times 10^{-4}$, $\bar{R}_N$ = 2 m, and $\epsilon = 0$.

with and without a stretched mesh for flow over a body described by the relation

$$x' = (r^2/2)/[1 + (r/2)\tan\theta_c] \tag{18}$$

where $\theta_c = 20°$. Near the nose, such a body is parabolic while as $r \to \infty$ the downstream portion of the body becomes conelike with a half-angle θ_c. Figure 3 shows a comparison of the resulting shock shapes, the solid line representing the solution using a tight mesh (15 mesh points to $x' = 4$), the symbols representing the solution using the expanded mesh (10 mesh points to $x' = 16$). The agreement is excellent. Note that in the vicinity of the nose of the vehicle, where flow properties change swiftly, the mesh is relatively closely spaced and that it opens up at locations farther downstream. Figure 4, for the same body and conditions, shows the pressure and tangential velocity distributions at the body surface. Here again the agreement is excellent and the expansion of the mesh as X, the tangential coordinate, increases can be clearly seen. A more subtle point to note is that the solutions agree well in the region where the more limited of the two is terminated. This generates confidence in the linear extrapolation procedures which are used to determine the flowfield properties at the most downstream mesh points.

Figure 5 is a comparison with the solution (no radiation) of Lomax and Inouye,[22] generally felt to be highly accurate. On Fig. 5 are shown the shock shapes about a 40° half-angle sphere-cone. The agreement is excellent, including the region near the expected shock inflection point shown in the enlarged view of the nose region. The solution of Ref. 22 consists, in the subsonic flow region, of an inverse iterative scheme which is joined with a characteristics solution for the supersonic flow downstream. Radiation cannot be treated. Figure 6, for the same conditions, compares the distribution of pressure and tangential velocity over the body. Over-all agreement is good with some discrepancy appearing in the pressures in the vicinity of the sphere-cone juncture, and attributed to the different means of handling this juncture in the two solutions.

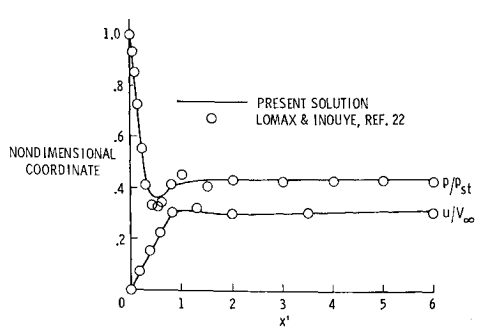

Fig. 6 Comparison of pressure and tangential velocity distribution over 40° sphere-cone; $\bar{V}_\infty$ = 12.2 km/sec, $\bar{\rho}_\infty/\bar{\rho}_0 = 2.24 \times 10^{-4}$, $\bar{R}_N$ = 2 m, and $\epsilon = 0$.

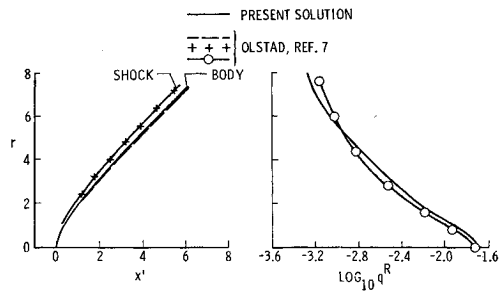

Fig. 7 Comparison of shock shape and radiative heating distribution with inverse solution; $\bar{V}_\infty$ = 12.2 km/sec, $\bar{\rho}_\infty/\bar{\rho}_0 = 2.24 \times 10^{-4}$, and $\bar{R}_N$ = 0.15 m.

In Fig. 7, an attempt is made to compare solutions with radiation with the work (based on Maslen's[12] technique) of Olstad.[7] This is made difficult by the fact that Olstad's solution is an inverse scheme and the present solution is not. However, on a trial and error basis, several body shapes were used in an attempt to obtain a shock closely approximating the input shock [Eq. (18)] of Olstad. From the standpoint of matching the entire shock, the attempt was not completely successful although a reasonable match is achieved over most of the downstream region. The result shows fair agreement in the body shapes. The radiative heat-transfer distribution, also shown on Fig. 7, shows reasonable agreement considering the imperfect shock-shape comparison and the completely different nature of the solutions. On Fig. 8, for the same case, enthalpy profiles, at the stagnation line and downstream, are compared. At the stagnation line the comparison is poor. This is expected since it is in this region that the assumptions inherent in the Maslen method break down. Downstream, however, agreement is excellent, effects of slight differences in δ being scaled out by the use of the normal coordinate y/δ.

On Fig. 9 are shown enthalpy profiles across the shock layer for two nose radii, two cone angles, and at two stations along the surface of the cone. For purposes of comparison, the adiabatic enthalpy profiles are shown with the dashed lines. As seen from Figs. 9a and 9b, nonadiabatic effects are important for both nose radii but, as expected, are far more severe for $\bar{R}_N$ = 2 m. The effect of cone angle on the enthalpy profile for $X = 0$ is, however, insignificant when standoff effects are scaled out. At the downstream station (X = 3.5), the difference between the 30° and 60° half-angle sphere-cones is clearly seen. For both nose radii, the 60° cone has a much higher enthalpy level through most of the shock layer reflecting the larger value of the local shock angle through which the flow passes. For $\bar{R}_N$ = 0.2m, the profiles are close to their adiabatic values for both cone angles except in the vicinity of the wall where the entropy layer has been significantly cooled by the radiative energy losses. Clearly, with a lower enthalpy level in the entropy layer, the vacuum

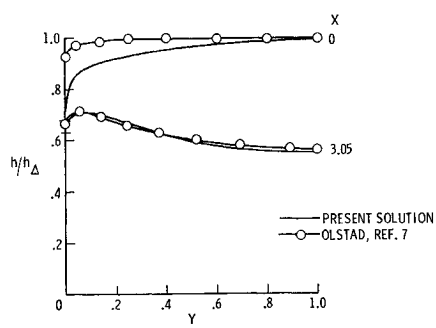

Fig. 8 Comparison of enthalpy profiles with inverse solution. $\bar{V}_\infty$ = 12.2 km/sec, $\bar{\rho}_\infty/\bar{\rho}_0 = 2.24 \times 10^{-4}$, and $\bar{R}_N$ = 0.15 m.

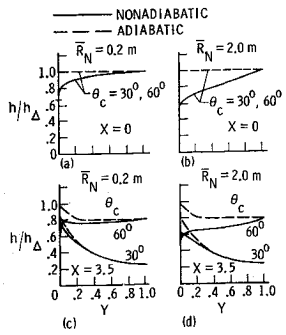

Fig. 9 Comparison of enthalpy profiles for sphere-cones; $\bar{V}_\infty$ = 12.2 km/sec, and $\bar{\rho}_\infty/\bar{\rho}_0 = 2.24 \times 10^{-4}$.

ultraviolet radiative contribution from this layer will be reduced. In addition, this reduced enthalpy level, in the region adjacent to the body, will be important in the computation of convective heating rates. For a nose radius of 2 m, Fig. 9d, the enthalpy profile for the 60° cone is significantly lower than the adiabatic profile through most of the shock layer. This causes a reduction in the radiative heating from both the optically thin and thick portions of the spectrum. For the 30° cone, differences are primarily in the region close to the body surface, once again the result of radiative cooling of the hot entropy layer.

Figure 10 shows the normalized nonadiabatic radiative heating distributions over sphere-cones for two nose radii and three cone angles. For $\bar{R}_N = 0.2$ and $\theta_c = 30°$ and 45°, the heating rates drop swiftly with X, reach a relatively low minimum, and very gradually rise. For $\theta_c = 60°$, the minimum heating occurs near the juncture of the sphere-cone after which q^R rapidly increases. This is a result of an increase in δ as X increases, coupled with the relatively high temperatures that exist behind an approximately 60° shock wave. Indeed, as X becomes larger q^R surpasses the stagnation value of $q_{st}{}^R$. For $\bar{R}_N = 2$ m, the relative effects are not greatly different for $\theta_c = 30°$ and 45°. The 60° cone, however, begins to display the effects of optical thickness as well as increased radiative cooling, q^R rising more slowly as X increases. Clearly, the radiative heating-rate distributions are highly nonsimilar with respect to variations in θ_c and $\bar{R}_N$.

One should note that though the ratios $q^R/q_{st}{}^R$ have approximately the same levels for both $\bar{R}_N$, the values of $q_{st}{}^R$ are greatly different. For the 60° cone, the values of $q_{st}{}^R$ are 0.0712 for $\bar{R}_N = 2$ m, and 0.0209 for $\bar{R}_N = 0.2$ m. The values of $q_{st}{}^R$ are approximately the same (within 1%) for $\theta_c = 30°$ and 45°.

Figure 11 illustrates dramatically the effect that radiative cooling has on the radiative heating-rate distribution. Shown are distributions of q^R about 60° sphere-cones for two nose radii. Clearly, even for the smaller nose radius, coupling between the radiative energy transport and the governing flowfield equations must be included if reasonable results are to be achieved. As an example of the differences that may result if coupling is ignored, for $\bar{R}_N = 2$m and for $X = 6$ there is a factor of 6 difference in the predicted value of q^R.

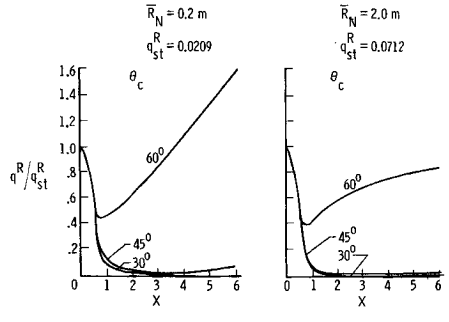

Fig. 10 Comparison of radiative heating distributions for sphere-cones. $\bar{V}_\infty$ = 12.2 km/sec and $\bar{\rho}_\infty/\bar{\rho}_0 = 2.24 \times 10^{-4}$.

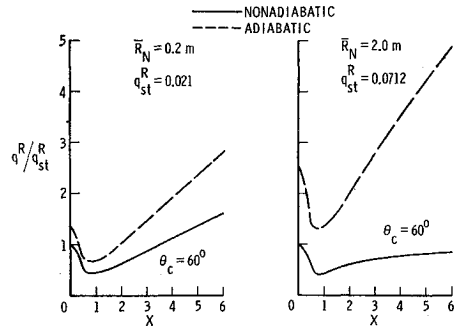

Fig. 11 Comparison of adiabatic and nonadiabatic radiative heating distributions for a sphere-cone; $\bar{V}_\infty$ = 12.2 km/sec and $\bar{\rho}_\infty/\bar{\rho}_0 = 2.24 \times 10^{-4}$.

Figure 12 illustrates, as a function of X, the relative or fractional contributions of the individual steps of the absorption coefficient to the radiative heat transfer. The figure is such that for a given X, the sum of the contributions of the various steps will be unity, the shaded area covering contributions less than 10% of the total. From this figure, it is evident that for the $\bar{R}_N$ and θ_c considered, steps 6 and 8 of the absorption coefficient are the dominant contributors for the range of X shown. Step 6 is composed of the wings of the vacuum ultraviolet lines and an underlying continuum. Step 8 includes the lines and underlying continuum in the visible and infrared portions of the spectrum. It should be noted that for the 30° cone, the radiative heat transfer is, as previously shown, almost negligible downstream of $X = 1$, so that what happens there is of little importance. For the 60° cone, however, this is not the case since the afterbody heating rate can be larger than that at the stagnation point. Steps other than 6 and 8 contribute, for the most part, less than 10% of the total, especially for the more optically thick calculations.

Concluding Remarks

The present analysis may be summarized with the following comments:

1) As a flowfield solution, the time asymptotic technique is an effective means of making second-order accurate calculations. The method is direct, proceeds from a specified body, and requires a modest amount of computer time and storage (~5 minutes on a CDC 6600 with 100 K core storage). The method is applicable in subsonic, supersonic, or mixed flow regions and the effects of emission and absorption of nongray radiation are easily taken into account. With the aid of a stretched mesh, flowfield calculations may be extended far downstream of the sonic line. Numerical instabilities present no problem. The analysis has been successfully applied to

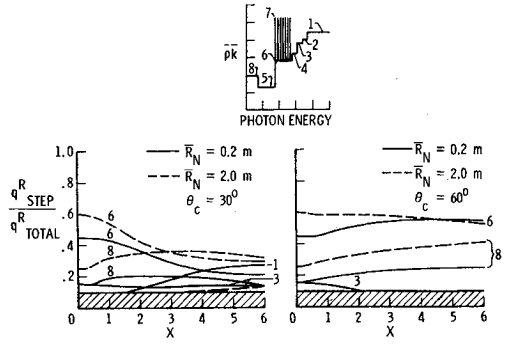

Fig. 12 Relative contribution of spectral steps to the radiative heating distribution for sphere-cones; $\bar{V}_\infty$ = 12 km/sec and $\bar{\rho}_\infty/\bar{\rho}_0 = 2.24 \times 10^{-4}$.

flow situations with $10 \leq \bar{V}_\infty \leq 18$ km/sec, $0.2 \leq \bar{R}_N \leq 5$ m, $36.55 \leq \bar{Z} \leq 73.1$ km, and $20° \leq \theta_c \leq 60°$.

2) The primary effect of radiation on flowfields over long blunted bodies is a general reduction, due to radiative cooling, of the enthalpy level in the shock layer. This effect is especially pronounced in the entropy layer, resulting in a significant decrease in the vacuum ultraviolet contribution of this layer to the radiative heating rate, q^R. For sphere-cones, the stagnation value of q^R is relatively insensitive to the afterbody cone angle θ_c while downstream, q^R is a strong and higher nonlinear function of θ_c. In fact, for larger cone angles, heating rates in excess of stagnation values can exist over a large portion of the afterbody posing serious thermal protection problems. In addition, the distribution of q^R is also strongly altered by the radiative cooling which occurs not only in the stagnation region, but also in the shock layer along the afterbody.

References

[1] Callis, L. B., "Solutions of Blunt-Body Stagnation-Region Flows With Nongray Emission and Absorption of Radiation by a Time Asymptotic Technique," TR R-299, Jan. 1969, NASA.

[2] Olstad, W. B., "Blunt-Body Stagnation-Region Flow With Nongray Radiation Heat Transfer—A Singular Perturbation Solution," TR R-295, Nov. 1968, NASA.

[3] Chin, J. H., "Radiation Transport for Stagnation Flows Including the Effect of Lines and Ablation Layer," AIAA Paper 68-664, Los Angeles, Calif., 1968.

[4] Page, W. A. et al., "Radiation Transport in Inviscid Nonadiabatic Stagnation-Region Shock Layers," AIAA Paper 68-784, Los Angeles, Calif., 1968.

[5] Wilson, K. H. and Hoshizaki, H., "A Study of Super-Orbital Heating Problems. Volume 1—Effect of Ablation Product Absorption and Line Transitions on Shock Layer Radiative Transport," 4-17-67-11, July 1968, Lockheed Missiles & Space Co., Sunnyvale, Calif.

[6] Cheng, P. and Vincenti, W. G., "Inviscid Radiating Flow Over a Blunt Body," *Journal of Fluid Mechanics*, Vol. 27, Pt. 4, March 1967, pp. 625–646.

[7] Olstad, W. B., "Nongray Radiating Flow About Smooth Symmetric Bodies With Large Blowing," AIAA Paper 69-327, San Francisco, Calif., 1969.

[8] Suttles, J. T., "A Method of Integral Relations Solution to the Nonadiabatic Radiation Problem for an Inviscid Blunt-Body Flow Field," M.S. thesis, 1968, Aeronautical Engineering Dept., Virginia Polytechnic Institute.

[9] Burns, R. K. and Oliver, C. C., "Downstream Radiation Flux to Blunt Entry Vehicles," *AIAA Journal*, Vol. 6, No. 12, Dec. 1968, pp. 2452–2453.

[10] Wang, K., "Radiating and Absorbing Steady Flow Over Symmetric Bodies," *Journal of Quantitative Spectroscopy and Radiative Transfer*, Vol. 8, No. 1, Jan. 1968, pp. 119–144.

[11] Hoshizaki, H. and Wilson, K. H., "Convective and Radiative Heat Transfer During Superorbital Entry," *AIAA Journal*, Vol. 5, No. 1, Jan. 1967, pp. 25–35.

[12] Maslen, S. H., "Inviscid Hypersonic Flow Past Smooth Symmetric Bodies," *AIAA Journal*, Vol. 2, No. 6, June 1964, pp. 1055–1061.

[13] Moretti, G. and Abbett, M., "A Time Dependent Computational Method for Blunt Body Flows," *AIAA Journal*, Vol. 4, No. 12, Dec. 1966, pp. 2136–2141.

[14] Ames, W. F., "Numerical Methods," *Nonlinear Partial Differential Equations in Engineering*, 1st ed., Academic Press, New York, 1965, pp. 438–440.

[15] Lax, P. D., "Weak Solutions of Nonlinear Hyperbolic Equations and Their Numerical Computation," *Communications on Pure and Applied Mathematics*, Vol. VII, No. 1, Feb. 1954, pp. 159–193.

[16] Lax, P. D. and Wendroff, B., "Difference Schemes for Hyperbolic Equations With High Order of Accuracy," *Communications on Pure and Applied Mathematics*, Vol. XVII, No. 3, Aug. 1964, pp. 381–398.

[17] Callis, L. B., "Time Asymptotic Solutions of Blunt-Body Stagnation-Region Flows With Nongray Emission and Absorption of Radiation," AIAA Paper 68-663, Los Angeles, Calif., 1968.

[18] Hahne, G. E., "The Vacuum Ultraviolet Radiation From N^+- and O^+-Electron Recombination in High Temperature Air," TN D-2794, 1965, NASA.

[19] Wilson, K. H. and Nicolet, W. E., "Spectral Absorption Coefficients of Carbon, Nitrogen, and Oxygen Atoms," *Journal of Quantitative Spectroscopy and Radiative Transfer*, Vol. 7, No. 6, Nov.-Dec. 1967, pp. 891–941.

[20] Cohen, N. B., "Correlation Formulas and Tables of Density and Some Transport Properties of Equilibrium Dissociating Air for Use in Solutions of the Boundary-Layer Equations," TN D-194, 1960, NASA.

[21] Cohen, N. B., "Boundary-Layer Similar Solutions and Correlation Equations for Laminar Heat-Transfer Distribution in Equilibrium Air at Velocities Up to 41,000 Feet Per Second," TR R-118, 1961, NASA.

[22] Lomax, H. and Inouye, M., "Numerical Analysis of Flow Properties About Blunt Bodies Moving at Supersonic Speeds in an Equilibrium Gas," TR R-204, 1964, NASA.